Skyrmion dynamics induced by surface acoustic waves in antiferromagnetic systems

Rohollah Khoshlahni,[1,2,*] Serban Lepadatu,[3] Majid Kouhi,[4] and Majid Mohseni[1,†]
[1]*Department of Physics, Shahid Beheshti University, Tehran 19839, Iran*
[2]*Institute for Advanced Studies in Basic Science (IASBS), Zanjan, Iran*
[3]*Jeremiah Horrocks Institute for Mathematics, Physics and Astronomy, University of Central Lancashire, Preston PR1 2HE, United Kingdom*
[4]*Ardabil Meteorological Administration, Ardabil, 5618413311, Iran*

(Received 25 January 2023; revised 27 March 2023; accepted 3 April 2023; published 19 April 2023)

In this paper, dynamics of a magnetic skyrmion induced by linear and circular surface acoustic waves in antiferromagnetic (AFM) systems are determined. The skyrmion is considered as a rigid disk with a repulsive constant potential that scatters the surface waves. By insertion of skyrmion profile inside the AFM Lagrangian, the equation of motion could be inferred. Conservation of linear and angular momenta results in a force and torque applied to the skyrmion by surface waves. The force and torque are calculated by using the scattering concept in the Born approximation for both linear and circular polarization. By equating the time derivative of these momenta with force and torque emerged from the Born approximation, the skyrmion dynamic is determined as a coupled nonlinear differential equation. The motion of skyrmion has no Hall effect in linear waves, confirming the physics of AFM skyrmion dynamics with no Magnus force. The skyrmion shows a ratchet motion in circular waves. This dynamic emerges because circular waves can produce a small amount of torque on spin texture. The velocity is inversely proportional to the Gilbert damping, as expected for AFM systems. We found meaningful consistency between our theoretical findings and atomistic simulation. Besides, we observe that the velocity goes up with skyrmion radius. Our findings uncover a nonlinear dynamics for skyrmions in AFM systems that can be originated by coupling to acoustic waves for future studies.

DOI: 10.1103/PhysRevB.107.144421

I. INTRODUCTION

One of the attractive subfields of magnetism is the antiferromagnetic (AFM) spintronics. AFMs' robustness against external magnetic-field perturbations, terahertz dynamics, absence of stray field, and low-power data transmission make them suitable materials for spintronic applications [1–8]. The first observation of AFMs comes back to the 1930s and lack of net magnetization made it difficult for applications in the past [9,10]. However, some theoretical and experimental works in controlling AFM spin textures such as domain walls (DWs) [11–14] brought them to the attention of scientists. One of their most important effects which provides exotic spin texture in AFMs is the Dzyaloshinskii-Moriya interaction (DMI) [15,16]. This is a peculiar symmetry breaking interaction arising from relativistic origin. It emerges from spin-orbit coupling in the bulk of noncentrosymmetric crystals such as metallic alloys with B20 structures [17–20] and in the surface of thin magnetic layers [21–23]. Unlike the exchange interaction, in which spins tend to be parallel, DMI forces the spins to configure in perpendicular direction. The competition between them along with anisotropy leads to formation of novel spin textures.

Skyrmions, being a topologically protected soliton, could be stabilized as a nanosize whirling spin texture in noncentrosymmetric magnetic materials [24–26]. The core reason for stabilization at the nanoscale is the inhomogeneous DMI in inversion asymmetric magnetic materials [27–33]. Isolated skyrmion creation and dynamics have been reported as a metastable state in both FM and AFM systems [34–39]. They are appropriate candidates for transmitting, encoding, and processing data in spintronic devices [40–42].

Skyrmions may be displaced by external perturbations such as electrical current [40,43–45], spin current [46–49], temperature gradient (incoherent magnons) [39,50,51], magnetic field, and anisotropy gradients [52,53].

Another external stimulus which can drive spin textures such as DWs [54–56] is surface acoustic waves (SAWs). Although skyrmion motion by SAWs has been studied by Nepal *et al.* [57] in FM systems, its dynamics has not been hitherto investigated in AFM insulators. Generally, skyrmion dynamics is explored as a particle-like rigid body by the Landau-Lifshitz-Gilbert (LLG) equation and, sequentially, by multiplying the appropriate term, turns it into collective coordinate, introduced by Thiele [58]. Although this method has its own advantages, it has some weaknesses that must be taken into account when applying it to real-world systems [59]. Since the Thiele approach satisfies the linear motion of the magnetic solitons, the higher-order terms are neglected. To study the nonlinear behavior of a magnetic soliton a new method is required.

*rkhoshlahn91@gmail.com
†m-mohseni@sbu.ac.ir

Here we formulate the skyrmion motion by scattering approach without using the LLG equation. Therefore, our method can be generalized to other solitons with a determined magnetic profile. In this paper we analytically explore the magnetization dynamics of an insulator AFM skyrmion under monochromatic linear and circular surface waves. Then, we verify our findings with numeric calculations based on the simulation of AFM skyrmion motion in a two-sublattice LLG equation.

The rest of this paper is organized as follows: In Sec. II we start from the AFM free energy and pertaining Lagrangian to obtain the skyrmion equation of motion (EOM). In Sec. III the total force and torque which is needed to solve the EOM is extracted from effective phonon Lagrangian in linear and circular wave polarization. In this section we demonstrate the conformation of numerical results with theoretical predictions. Finally, we present the paper's outcomes and results in Sec. IV and propose ideas for future works.

II. THEORY AND MODEL: ANTIFERROMAGNETIC SYSTEMS

The effective thermodynamic free energy for a two-dimensional square lattice antiferromagnetic system may be considered as

$$\mathrm{U}[\mathbf{S}_i,\mathbf{S}_j]=\sum_{\langle i,j\rangle}J_{i,j}\mathbf{S}_i\cdot\mathbf{S}_j-\sum_{\langle i,j\rangle}\mathbf{D}_{i,j}\cdot\mathbf{S}_i\times\mathbf{S}_j-K\sum_i(S_z)^2-\sum_i\mathbf{H}\cdot\mathbf{S}_i, \tag{1}$$

where $\mathbf{S}_{i,j}$ is the spin magnetic moment at sites i, j. The terms are the Heisenberg exchange interaction with $J>0$ for nearest neighbor, DMI with $D_{i,j}$ vector, uniaxial anisotropy with $K<0$ and Zeeman, respectively. The $J>0$ exchange interaction encourage adjacent spins to be antiparallel with each other, the DMI forces them to become perpendicular and magnetic anisotropy prefers to be in a special direction in a crystal. The long-range dipolar interaction can be ignored because, in ultrathin magnetic systems with no net magnetization, the interaction is negligible. Topological magnetic textures, such as DWs, skyrmions [24,60], bimerons [61,62], and hopfions [63,64] are created through the interplay of these energies both in ground states and metastable states.

To study the underlying interactions in magnetic systems, one can transfer to the continuum model for each sublattice. In this case the free energy of an AFM system is intuitively considered as superposition of each sublattice magnetization [65,66]. An AFM system consists of two FM sublattices with normalized order parameter $|\mathbf{m}_i|=1$, $i=1,2$ for each sublattice. Therefore the superposed free energy that satisfies the symmetry of bipartite AFM can be phenomenologically written as

$$\begin{aligned}\mathrm{U}[\mathbf{m}_1,\mathbf{m}_2]=\int dV\big\{&B((\nabla\mathbf{m}_1)^2+(\nabla\mathbf{m}_2)^2)\\&+B'(\nabla\mathbf{m}_1\cdot\nabla\mathbf{m}_2)+b\,\mathbf{m}_1\cdot\mathbf{m}_2\\&-(\mathbf{m}_1+\mathbf{m}_2)\cdot\mathbf{H}-\mathcal{K}\big(m_{1z}^2+m_{2z}^2\big)\\&-\mathcal{K}'m_{1z}m_{2z}+w_D'+w_D\big\}.\end{aligned} \tag{2}$$

In Eq. (2) the free energy consists of Heisenberg exchange coupling with inhomogeneous (B, B') and homogeneous (b) coefficients. The Zeeman interaction affects both sublattices separately so that the external magnetic field $\mathbf{H}$ is factored out. The uniaxial second-order magneto-crystalline anisotropies are displayed by the next two terms with $\mathcal{K}$, $\mathcal{K}'$ coefficients, where the z axis is the normal direction of AFM surface. The remaining two terms are the homogeneous and nonhomogeneous DM interaction, which create *weak ferromagnetism* [1,6,67–69] and chiral helimagnets [70–75], respectively. The homogeneous DM interaction is the reason for *weak ferromagnetism* and the inhomogeneous term which exists in noncentrosymmetric crystals results in chiral structures in magnetic materials [76–80]. The antiparallel construction of magnetic moments in AFM sublattices leads to the compensation of magnetic moments on atomic scales and consequently stray field contribution in magnetic free-energy vanishes. The former property makes the AFM systems to be promising for spintronics.

The force and torque applied to an antiferromagnetic skyrmion

Well below the Néel temperature the AFM order parameter unit vector, staggered magnetization, is $\mathbf{n}(\mathbf{r},t)=\mathbf{l}(\mathbf{r},t)/|\mathbf{l}(\mathbf{r},t)|$ in which $\mathbf{l}(\mathbf{r},t)=(\mathbf{m}_1-\mathbf{m}_2)/2$ is the difference in the sublattice's order parameter and $\mathbf{m}(\mathbf{r},t)=(\mathbf{m}_1+\mathbf{m}_2)/2$ is the total magnetization for an AFM system, where $|\mathbf{l}(\mathbf{r},t)|\approx 1$ and $\mathbf{m}\ll\mathbf{l}$ so that these terms bring the $\mathbf{n}\cdot\mathbf{m}=0$ and $\mathbf{n}^2+\mathbf{m}^2=1$ constraints. While in the equilibrium phase $\mathbf{m}_1$ and $\mathbf{m}_2$ are antiparallel, $|\mathbf{m}_1(\mathbf{r},t)|=|\mathbf{m}_2(\mathbf{r},t)|=1$. However *weak ferromagnetism*, small magnitude total magnetization emerges from small deviations of the sublattice's magnetization in typical AFMs.

To simplify the study of AFM systems one can transfer from the two-sublattice state to the total and staggered magnetization framework as mentioned above:

$$\mathrm{U}[\mathbf{n},\mathbf{m}]=\int dV\left[\frac{a}{2}|\mathbf{m}|^2+\frac{A}{2}(\nabla\mathbf{n})^2-\frac{K}{2}n_z^2+w_D\right], \tag{3}$$

where a, A, and K are the homogeneous, inhomogeneous exchange, and uniaxial anisotropy constants, respectively [81,82]. The energy density of the bulk DMI may be written as $w_D=\mathrm{D}\mathbf{n}\cdot(\boldsymbol{\nabla}\times\mathbf{n})$ which stabilizes Bloch skyrmions in noncentrosymmetric materials such as MnSi and FeGe [18,19,83]. Furthermore it takes the form of $w_D=\mathrm{D}[(\mathbf{n}\cdot\hat{z})(\boldsymbol{\nabla}\cdot\mathbf{n})-(\mathbf{n}\cdot\boldsymbol{\nabla})(\mathbf{n}\cdot\hat{z})]$ for the interfacial DMI creating Néel skyrmion [40,84]. The staggered and total magnetization definitions for the order parameters and that the leading term in AFM free energy is the exchange interaction bring some simplifications to the formulas. Therefore, in the exchange approximation the total magnetization derivatives may be neglected. Besides, the intrinsic magnetization field can be written in terms of Néel magnetization temporally and spatially which means that it is a slave variable, $\mathbf{m}\propto(\dot{\mathbf{n}}\times\mathbf{n}+\boldsymbol{\nabla}\mathbf{n})$ [82]. For the study of staggered magnetization dynamics we use the Lagrangian approach here [85–87]. Moreover, we can deduce the force and torque from modified Lagrangian density for the mechanical waves [88] containing magnetic effects [54]. The total AFM Lagrangian, is the difference between the kinetic energy and the thermodynamic free energy. The AFM

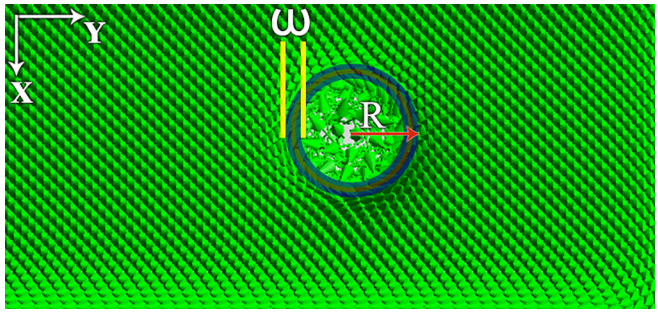

FIG. 1. The schematic shape of an AFM skyrmion with radius R and wall ω. The wall thickness is shown with a transparent thin layer where the direction of staggered magnetization changes.

Lagrangian reads [14,89–93]

$$\mathcal{L} = \frac{\mathcal{A}}{2}\int \dot{\mathbf{n}}^2\, d^2\mathbf{r} - \mathrm{U}[\mathbf{n}], \tag{4}$$

where $\mathcal{A} = M_0/(\gamma^2 H_{exc})$ is the inertia of AFM order parameter and the dot sign shows the time derivative. Other parameters such as M_0, H_{exc}, and γ are saturation magnetization, the exchange field containing the Heisenberg interaction and gyromagnetic ratio, respectively [82,94,95]. The free energy contribution, $\mathrm{U}[\mathbf{n}] = \frac{A'}{2}|\nabla\mathbf{n}|^2 - \frac{K}{2}n_z^2 + w_D$, contains topological coefficient in A', however, the related term is disregarded. Furthermore, the homogeneous DMI is neglected because they have no effect on the equation of motion [96]. The magnetization stationary state satisfying the AFM free energy is given by $\mathbf{n}(\mathbf{r}) = (\sin\theta(r)\cos\phi(\varphi),\ \sin\theta(r)\sin\phi(\varphi),\ \cos\theta(r))$ so that for the skyrmion $\theta(r)$ and $\phi = \delta\varphi + \beta$ determine the texture profile and topological number [97] with boundary values of $\theta(r = 0) = \pi, (0)$ and $\theta(r \longrightarrow \infty) = 0, (\pi)$. δ is the vorticity of skyrmion and $\beta = 0, \pi$ and $\beta = \pm\frac{\pi}{2}$ show the Néel- or Bloch-type skyrmion, respectively. In our calculations we assume $\delta = 1$ and $\beta = 0$.

To study the skyrmion dynamics the polar component of magnetization can be considered as a 360° domain wall [98,99] and the time dependency is introduced as,

$$\theta(r,t) = 2\arctan\left[\frac{\sinh\frac{R}{\omega}}{\sinh\left(\frac{r-\rho(t)}{\omega}\right)}\right], \tag{5}$$

in which R, ω, r, and $\rho(t)$ are the radius, thickness of the skyrmion wall, internal coordinate of the lattice atoms, and the position of skyrmion center, respectively. The skyrmion profile is schematically displayed in Fig. 1. Inserting Eq. (5) into Eq. (4) gives the Lagrangian in terms of polar and azimuthal coordinate as

$$\mathcal{L} = \frac{\mathcal{A}}{2}\int (\dot{\theta}^2 + \dot{\phi}^2\sin^2\theta)d^2\mathbf{r} - \mathrm{U}[\mathbf{n}]. \tag{6}$$

By changing variables as $y = [r - \rho(t)]/\omega$, $x = R/\omega$ (here x, y are not Cartesian coordinates) and assuming that $R \gg \omega$ $(x \gg 1)$ one can write $\sinh(x) \approx \cosh(x) \approx e^x$ [98], so by inserting the time derivative of $\theta(r, \rho(t))$ and $\sin\theta(r, \rho(t))$ in the Lagrangian we have

$$\mathcal{L} = 2\pi\mathcal{A}\omega\left(\frac{\dot{\rho}^2}{\omega^2} + \dot{\phi}^2\right)[R + \rho(t)] - \mathrm{U}[\mathbf{n}], \tag{7}$$

therefore the force and torque extracted from the Lagrangian become

$$\mathrm{f}_\rho = \dot{\mathrm{p}}_\rho = \frac{4\pi\mathcal{A}}{\omega}\{[R + \rho(t)]\ddot{\rho} + \dot{\rho}^2\}, \tag{8}$$

$$\tau = \dot{\mathrm{p}}_\phi = 4\pi\mathcal{A}\omega\{[R + \rho(t)]\ddot{\phi} + \dot{\rho}\dot{\phi}\}. \tag{9}$$

The expression for Rayleigh dissipation function is $\mathcal{R}(\dot{\mathbf{n}}) = \frac{\alpha M_0}{2\gamma}\int \dot{\mathbf{n}}^2 d^2\mathbf{r}$, and except for a coefficient it is the same as Lagrangian kinetic term. Consequently, the dissipative force and torque read

$$\mathrm{f}_\rho^{\mathcal{R}} = \frac{\partial\mathcal{R}}{\partial\dot{\rho}} = \frac{4\pi\alpha M_0}{\gamma\omega}[R + \rho(t)]\dot{\rho}, \tag{10}$$

$$\tau^{\mathcal{R}} = \frac{\partial\mathcal{R}}{\partial\dot{\phi}} = \frac{4\pi\alpha M_0}{\gamma}\omega[R + \rho(t)]\dot{\phi}. \tag{11}$$

The total force and torque felt by the skyrmion can be written from Eqs. (8) to (11) as

$$\begin{aligned}\mathrm{F}_{\mathrm{tot}} &= \frac{4\pi\mathcal{A}}{\omega}\{[R + \rho(t)]\ddot{\rho} + \dot{\rho}^2\} + \frac{4\pi\alpha M_0}{\gamma\omega}[R + \rho(t)]\dot{\rho},\\ \mathfrak{T}_{\mathrm{tot}} &= 4\pi\mathcal{A}\omega\{[R + \rho(t)]\ddot{\phi} + \dot{\rho}\dot{\phi}\} + \frac{4\pi\alpha M_0}{\gamma}\omega[R + \rho(t)]\dot{\phi}.\end{aligned} \tag{12}$$

In this section we deduced the equation of motion in radial and azimuthal directions with unknown total force and torque. In the next section the force and torque will be obtained from the phonon Lagrangian.

III. FORCE AND TORQUE EXTRACTED FROM PHONON LAGRANGIAN

A. Linear wave

To find the total force and torque we proceed as follows: In our model a two-dimensional ultrathin and narrow AFM nanosheet containing an isolated skyrmion is located on the x-y plane with uniaxial anisotropy in the z direction. However, the width of the nanosheet is wide enough to show the lateral motion of the skyrmion in the x direction. In the uniform state the effective Lagrangian density for the mechanical waves comprising magnetic effects is given by $L_{\mathrm{eff}} = \mu[\dot{\Phi}_1^2(y,t) + \dot{\Phi}_2^2(y,t)] - \mathcal{T}_{\mathrm{mag}}[\Phi_1'^2(y,t) + \Phi_2'^2(y,t)]$ [54] in which μ, $\mathcal{T}_{\mathrm{mag}}$ and the prime mark are the mass density of the sample, the applied tension, and the derivative with respect to internal degree of freedom, respectively. The magnetic effects have been included in the latter coefficient. $\Phi_1(y)$ and $\Phi_2(y)$ show the transverse vibration of the nanosheet in the x, z directions and y is the internal degree of freedom for lattice atoms along the wave-propagation direction.

Phonons have orbital angular momentum in magnetic crystals [100] so they can apply a torque on magnetic textures. Conservation of the momenta are deduced from the axial symmetry of the Lagrangian. Therefore, the phonons' orbital angular momentum current can be extracted from $\mathbf{I}^s = -\mathcal{T}_{\mathrm{mag}}[\Phi_1(y,t) + \Phi_2(y,t)]\times[\Phi_1'(y,t) + \Phi_2'(y,t)]$ which exerts torque on the skyrmion [100]. Meanwhile, the linear momentum current can be obtained from the energy-momentum tensor as $T^{11} = \mu[\dot{\Phi}_1(y,t)^2 + \dot{\Phi}_2(y,t)^2]/2 + \mathcal{T}_{\mathrm{mag}}[\Phi_1'(y,t)^2 + \Phi_2'(y,t)^2]/2$.

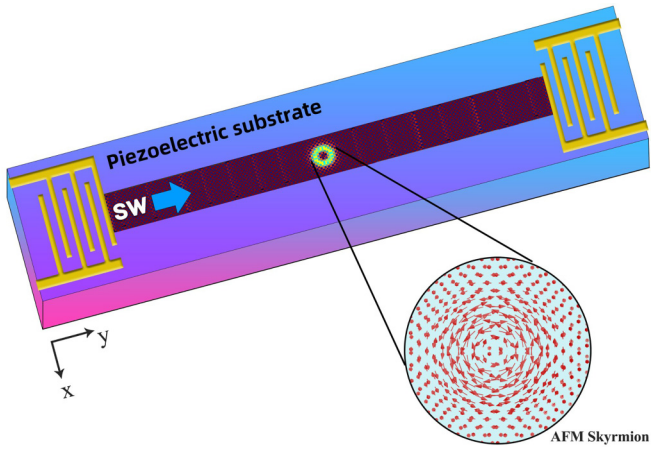

FIG. 2. Top view of schematic sketch of IDTs, piezoelectric substrate, and an AFM nanolayer containing a skyrmion. Surface wave is created by the left IDT and transmits through the nanolayer, then collides with skyrmion. The green color shows the wall of skyrmion that the z component of magnetization is zero. The zoomed view of skyrmion is displayed in a circle.

The torque is the difference in the angular momentum current $\mathbf{I}^s$, and the force is the difference in the linear momentum current T^{11} between the scattered and incident phonons, respectively. Figure 2 displays a sketch of a skyrmion on an AFM system containing the surface wave. The sample comprises two interdigitated transducer (IDT) electrodes to produce SW in the y direction from left to right [101]. The skyrmion has been created in the middle of the sample whose zoomed shape has been shown. The incident waves coming from the left electrodes collide with the skyrmion and get scattered so that it transmits the energy and momentum to the skyrmion, resulting in the linear and ratchet motion of the skyrmion in the different cases of wave polarization.

In the following we obtain the scattered wave for the linear case by means of the Born approximation [102]. The topology of the skyrmion ensures that its magnetization cannot be smoothly transformed into the uniform background magnetization, resulting in a characteristic size and shape that are independent of the details of the material. Therefore the skyrmion is considered as a magnetic defect with a definite profile, a robust topology and no deformation so that it operates as a blockade against the incident wave. With the mentioned characteristics, we consider the skyrmion as a hard disk-like scatterer potential, $V(\mathbf{r}') = \mathrm{t}V_0\delta(z')H(r'-R)$ where t, V_0, $\delta(z')$, and $H(r'-R)$ are the sample thickness, the potential constant, the Dirac δ function, and the step function, respectively. The parameter V_0, here, corresponds to the impulse strength of the interaction between the scatterer potential and the wave so that it has nothing to do with magnetoelastic coefficients. They are material dependent parameters and changing V_0 alters the scale of interaction between magnetic defect and the incoming wave.

The incident phonon wave is, $\Phi_{\mathrm{inc}}(\mathbf{x}) = ae^{i(\mathbf{k}\cdot\mathbf{x})}$. So the scattered plane wave is

$$\tilde{\Psi}_{\mathrm{sca}}(r) = \Phi_{\mathrm{inc}}(r) - \frac{e^{\mathrm{ikr}}}{r}f(x') \approx \Phi_{\mathrm{inc}}(r) - \frac{atmV_0\mathrm{A}}{2\pi\hbar^2}\frac{e^{\mathrm{ikr}}}{r}, \tag{13}$$

where t, m, V_0, a, and A are the sample thickness, sample atomic mass, potential constant, amplitude of the incident wave, and skyrmion area in the maximum scattering rate, respectively. In Eq. (13) we utilized the approximation of $[RJ_1(qR)]/q \approx R^2/2$, in which $J_1(qR)$ is the first-order Bessel function and $q = 2k$ is the difference of incident and scattered wave vector in the maximum scattering angle. We insert the scattered wave $\tilde{\Psi}_{\mathrm{sca}}(r)$ in $\mathbf{I}_s$ and T^{11} to obtain the angular and linear momentum current. For the plane wave $\mathbf{I}_s = 0$, so the total torque vanishes: $\mathfrak{T}_{\mathrm{tot}} = \mathbf{I}_{\mathrm{sca}} - \mathbf{I}_{\mathrm{inc}} = 0$. The total force and time-averaged linear momentum current differences for maximum scattering rate reads,

$$\begin{aligned}\mathbf{F}_{\mathrm{tot}} &= T^{11}_{\mathrm{sca}} - T^{11}_{\mathrm{inc}} \\ &= -\mathcal{T}_{\mathrm{mag}}(|\tilde{\Psi}'_{\mathrm{sca}}(r)|^2 - |\Phi'_{\mathrm{inc}}(r)|^2) \\ &\approx \frac{\mathcal{T}_{\mathrm{mag}}a^2mt}{r\hbar^2}k^2R^2V_0. \end{aligned} \tag{14}$$

Therefore, the skyrmion dynamics that is shown in Eq. (12) can be written as a coupled nonlinear differential equation,

$$\Re(t)\ddot{\Re}(t) + \dot{\Re}(t)^2 + \frac{\alpha M_0}{\gamma\mathcal{A}}\Re(t)\dot{\Re}(t) = \frac{\omega\mathbf{F}_{\mathrm{tot}}}{2\pi\mathcal{A}}, \tag{15}$$

$$\ddot{\phi}(t) + \left(\frac{\dot{\Re}(t)}{\Re(t)} + \frac{\alpha M_0}{\gamma\mathcal{A}}\right)\dot{\phi}(t) = \frac{\mathfrak{T}_{\mathrm{tot}}}{4\pi\mathcal{A}\omega\Re(t)} \tag{16}$$

where $\Re(t) = R + \rho(t)$ and the initial velocities are zero in both directions. Then, the dynamics of radial and azimuthal component of the skyrmion reads,

$$\dot{\Re}(t) = \frac{b(1-e^{-\mathrm{a}t})}{2[b(\mathrm{a}t + e^{-\mathrm{a}t} - 1) + \mathrm{a}^2R^2]^{1/2}}, \tag{17}$$

then

$$\Re(t) = \frac{\sqrt{b(\mathrm{a}t + e^{-\mathrm{a}t} - 1) + \mathrm{a}^2R^2}}{\mathrm{a}}, \tag{18}$$

$$\dot{\phi}(t) = \frac{\mathrm{V}_{0\phi}Re^{-\mathrm{a}t}}{\Re(t)} - \mathrm{V}_{0\phi} \text{ for } \mathfrak{T}_{\mathrm{tot}} = 0. \tag{19}$$

Here $b = \omega\mathbf{F}_{\mathrm{tot}}/(2\pi\mathcal{A})$ and $\mathrm{a} = \alpha M_0/(\gamma\mathcal{A})$. Then we present its dynamics in radial direction (here this is in the y direction). To obtain the AFM skyrmion motion affected by elastic wave we consider the sample width of 100 nm and length of 1 μm subjected to $\mathcal{T}_{\mathrm{mag}} = 10^{-3}$ N of tension. We assume that the IDTs can produce a typical wave vector $k = 1.2\times10^7$ m^{-1}. The wave amplitude order of magnitude is assumed to be half of the lattice spacing d, and the atomic mass of sample is equal to iron case, m = 55 amu (atomic mass units) [103]. The range of skyrmion repulsive potential as a hard circular barrier changes from $V_0 = 15\times10^{-4}$ to 260×10^{-4} eV. The radius of the skyrmion depends on the magnetic parameters of the system; that is, the exchange, anisotropy, DMI, and external magnetic field. We note that experimental values range from 1.5 to 2000 nm [104–108]. Consequently, for a skyrmion with $R = 10$ nm the total force is brought out as $\mathbf{F}_{\mathrm{tot}} = 3.3\times10^{18}V_0$. To visualize the topological texture dynamics we consider two different Gilbert damping constants as $\alpha = 0.01,\ 0.02$ and skyrmion wall thickness $\omega = R/10$ in a constant wavelength $\lambda = 525$ nm. Based on mentioned magnitudes, the temporal $\dot{\rho}(t)$ diagram is displayed in Fig. 3.

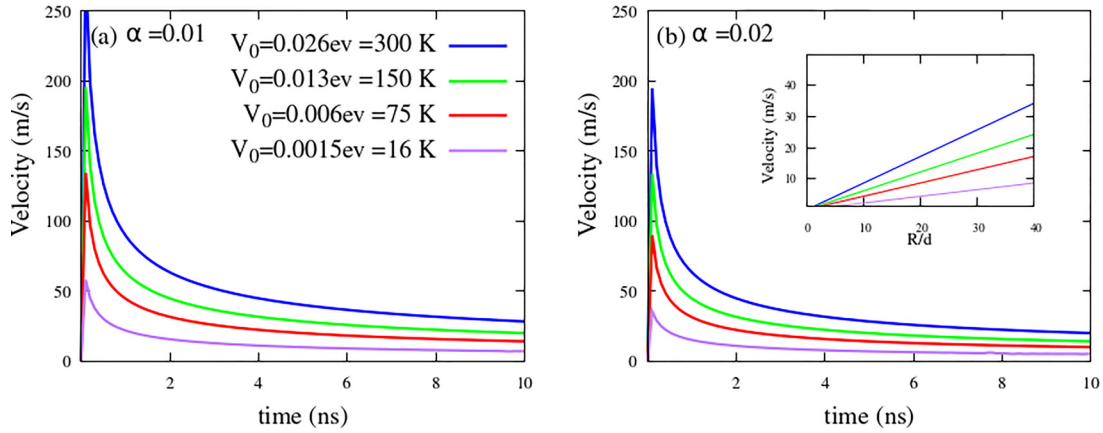

FIG. 3. Dynamics of skyrmion in ρ direction, here is the direction of incident wave in y direction, for constant wavelength $\lambda = 525$ nm. (a) Skyrmion velocity changes with potential strength. The potentials start from 15×10^{-4} to 260×10^{-4} eV. Gilbert damping is $\alpha = 0.01$. (b) By doubling the Gilbert damping the velocity decreases for the same potentials. The inset displays velocity increment with the ratio of radius to lattice spacing, R/d, for various repulsive potentials.

As the chart displays, the velocity of the skyrmion skyrockets from zero to a peak in a very small time span. It seems that the instantaneous interaction between wave and skyrmion leads to an abrupt movement of the skyrmion and the transmission of momentum takes place. Then, the skyrmion velocity decreases gradually and approaches the asymptotic value. The velocity reduces for two reasons: On the one hand, the mechanical damping η results in energy loss. On the other hand, the Gilbert damping α also results in energy dissipation, and therefore these resistant forces hinder the skyrmion dynamics and lead to velocity subsiding. To show the practicality of the repulsive hard-disk-like potential, the temperature equality is written on the diagram. As the hardness of the skyrmion as a repulsive potential rises, the peak and asymptotic velocity increase, which is apparent in Fig. 3(a). Both Fig. 3 and Eq. (17) show that the dynamics in the radial direction are inversely proportional to Gilbert damping. The effect of viscous force increment is clearly observed in Fig. 3(b) in which the inverse proportionality is obvious. The steady-state motion of the AFM skyrmion reads $\dot{\rho}(t) \approx \mathrm{F_{tot}}\gamma\omega/(2\alpha \mathrm{M_0}\ell)$ where ℓ is the skyrmion perimeter. In the domain wall case as a potential barrier the perimeter has been canceled [54]. The boundary condition for the velocity in lateral direction confirms that the velocity vanishes in that direction. On the other hand, the physics of AFM systems has displayed the zero transverse velocity since the Magnus force is compensated in opposite directions [109], affirming that the AFM systems have no skyrmion Hall effect. Therefore, the skyrmion travels in a perfectly straight trajectory along the same direction as the incident wave. The velocity and the size of skyrmion correlation is presented in the inset. The velocity of the skyrmion linearly depends on the skyrmion radius and it increases with the skyrmion area.

The displacement of the skyrmion, here in the y direction, is shown in Fig. 4 in the repulsive potential of the skyrmion, $V_0 = 0.026$ eV, the damping of $\alpha = 0.01$, 0.02 and for different incident wavelengths. As depicted, with the increment of the damping coefficient the slope of the lines decreases confirming our previous findings. On the other hand, Fig. 4 displays the effect of waves created by IDTs on skyrmion motion. The skyrmion's motion is slower for smaller wave vectors and, as λ becomes smaller, the skyrmion moves faster. In this section we show the skyrmion dynamics in the presence of a linear wave. The equations and graphs affirm that the texture dynamics is directly proportional to the wave vector, potential, and radius and inversely is proportional to the Gilbert damping. In the next section we discuss the circular wave interaction with the skyrmion.

B. Circular wave

The incoming circular wave takes the form

$$\begin{aligned}\Phi_{\mathrm{inc}} &= \Phi_1(y,t)\hat{p} + \Phi_2(y,t)\hat{s}\\ &= a\cos(ky-\omega t)\hat{p} - a\sin(ky-\omega t)\hat{s},\end{aligned} \tag{20}$$

where $\hat{p}$ and $\hat{s}$ are orthogonal in the arbitrary directions. In the same way, the outgoing wave in elastic scattering reads

$$\begin{aligned}\tilde{\Psi}_{\mathrm{sca}} &= \Phi_{\mathrm{inc}} - \pi\frac{2mV_0 ta}{4\pi\hbar^2}\frac{e^{\mathrm{ikr}}}{r}\\ &\quad\times\left[\hat{p}\left(\frac{RJ_1(2kR)}{2k}+\frac{R^2}{2}\right)+i\hat{s}\left(\frac{RJ_1(2kR)}{2k}-\frac{R^2}{2}\right)\right]\\ &\approx \Phi_{\mathrm{inc}} - \frac{2mV_0 \mathrm{taA}}{4\pi\hbar^2}\frac{e^{\mathrm{ikr}}}{r}\hat{p}.\end{aligned} \tag{21}$$

The component in the $\hat{s}$ direction is removed since we consider only the first term of the Bessel function. By the same procedure, Eq. (14) gives the total force for the circular wave as

$$\mathbf{F}_{\mathrm{tot}} = T^{11}_{\mathrm{sca}} - T^{11}_{\mathrm{inc}} \approx \frac{\mathcal{T}_{\mathrm{mag}}a^2 mt}{2r\hbar^2}k^2R^2V_0. \tag{22}$$

Similarly the dynamics in the radial direction is the same as Eq. (15) but the magnitude of $\mathbf{F}_{\mathrm{tot}}$ is half of the previous magnitude because of the trigonometric function averaging. Therefore, it can be referred to Figs. 3 and 4 to study the circular-wave impact on skyrmion behavior in the radial direction.

The difference between a right and left phonon's orbital angular momentum current gives the torque, which is written

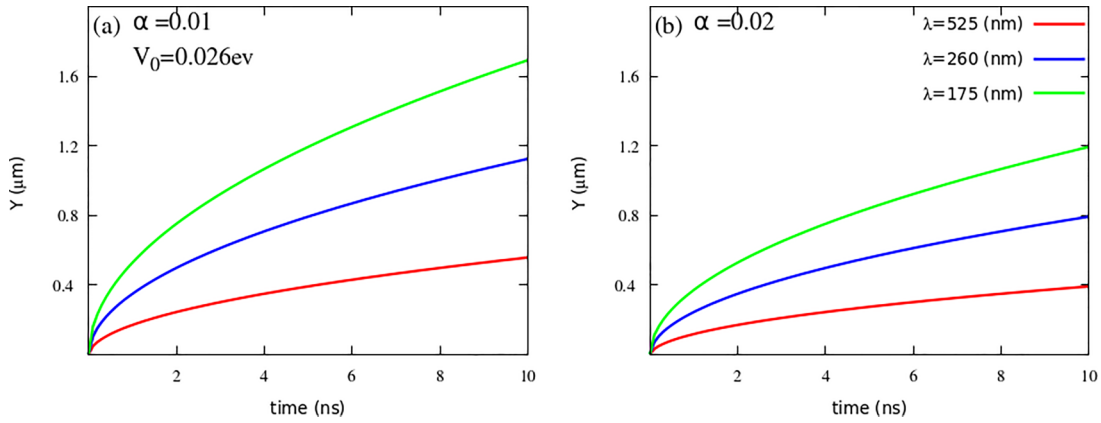

FIG. 4. The skyrmion position in the y direction and in the repulsive potential of $V_0 = 0.026$ eV. (a) The motion of the skyrmion is affected by the wavelength. Low wavelength has high impact on skyrmion motion. (b) Increasing the damping leads to slower skyrmion motion.

as

$$\begin{aligned}\mathfrak{T}_{\rm tot} &= \mathbf{I}_{\rm sca} - \mathbf{I}_{\rm inc} \\ &= -\mathcal{T}_{\rm mag}(\Psi_{\rm sca}\times\Psi'_{\rm sca} - \Phi_{\rm inc}\times\Phi'_{\rm inc}) \\ &= -\frac{\mathcal{T}_{\rm mag}a^2 mt}{2r\hbar^2}kR^2V_0. \end{aligned} \tag{23}$$

However, for the azimuthal component, the nonzero $\mathfrak{T}_{\rm tot}$ changes the skyrmion behavior. In the gigahertz order the ratio of $\dot{\Re}(t)/\Re(t) \approx 1/2t$ and $\Re(t) \approx \sqrt{\frac{b}{\rm a}t}$. Therefore, Eq. (16) for the circular wave can be written as

$$\ddot{\phi}(t) + \left(\frac{1}{2t} + {\rm a}\right)\dot{\phi}(t) = \frac{\mathfrak{T}_{\rm tot}}{4\pi\mathcal{A}\omega\sqrt{\frac{b}{\rm a}t}}, \tag{24}$$

$$\dot{\phi}(t) = \frac{\mathfrak{T}_{\rm tot}}{4\pi\mathcal{A}\omega\sqrt{ab}}\frac{(1-e^{-at})}{\sqrt{t}}. \tag{25}$$

This torque results in an ultrafast ratchet motion [110] of the skyrmion which is tunable with repulsive potential and Gilbert damping. Apparently, the angular velocity is proportional to the torque generated by a circular wave. As displayed in Fig. 5, the angular velocity plummets as the time elapses then it goes up to an asymptotic value. Figure 5(a) shows the velocity for damping $\alpha = 0.01$ and Fig. 5(b) is for damping $\alpha = 0.02$. The repulsive potential has a considerable role in the dynamics of the skyrmion. The diminishing potential leads to slower rotation of the skyrmion showing the low transfer of angular momentum to the texture. Unlike the linear wave, the scattering with circularly polarized surface waves can give rise to accumulation of angular momentum inside the skyrmion, which in turn causes the rotation of spins at the angular velocity proportional to the accumulated angular momentum. The saturation value for the angular velocity is of the order of $O(10^{13}\ {\rm s}^{-1})$ which is accessible in ferrimagnetic domain walls [111]. The direction of skyrmion rotation depends on the handedness of the incident circular wave, as is obvious in Eq. (20). The direction of angular velocity is determined by the helicity of surface waves. Provided that we ignore the timescale of skyrmion rotation and transmission, there is a similarity between the rotational and directional dynamics of the skyrmion. In both cases, there exists a mobility in the time span of wave and

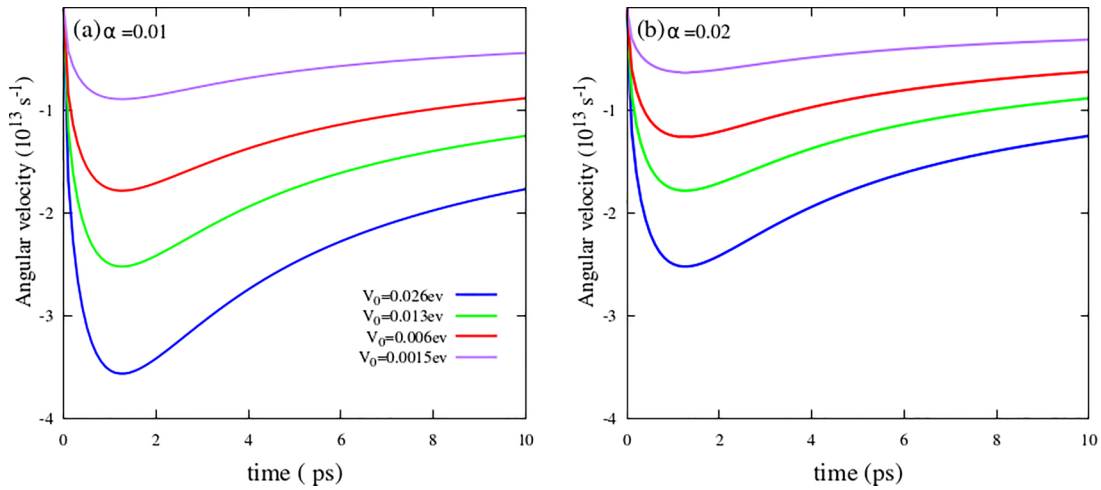

FIG. 5. The skyrmion angular velocity in different repulsive potentials of $V_0 = 0.026$ to 0.0015 eV. (a) The skyrmion experiences a higher magnitude of rotation around its central axis in small damping, $\alpha = 0.01$. (b) The magnitude of angular velocity reduces with increment of Gilbert damping, $\alpha = 0.02$.

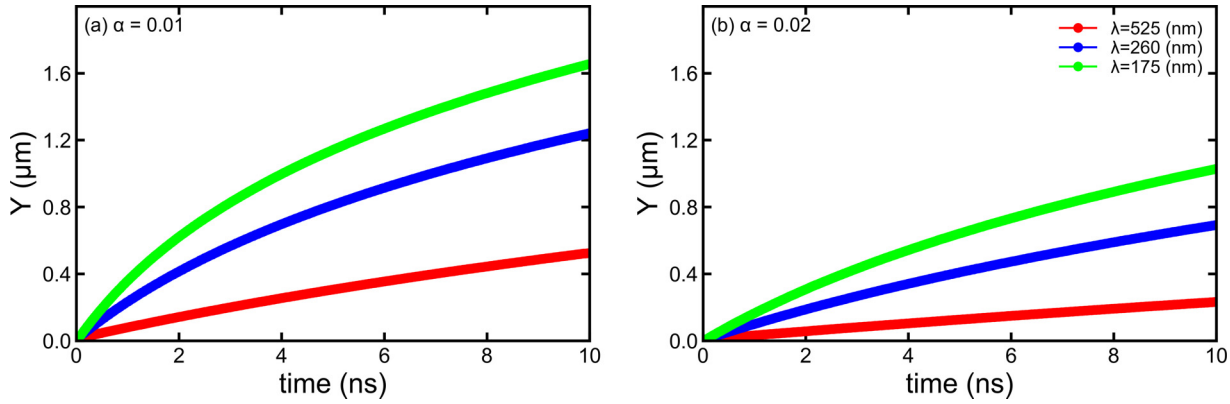

FIG. 6. Skyrmion position as a function of time, computed numerically for linear waves with wavelengths $\lambda = 175$, 260, and 525 nm, and magnetic damping parameters of (a) $\alpha = 0.01$ and (b) $\alpha = 0.02$.

skyrmion collision. After that, the dynamics goes to a steady state and approaches uniform motion. This demonstrates that the transfer of linear and angular momentum takes place in a small interval of time, in contrast to the stationary state.

C. Simulation of skyrmion dynamics

To verify the analytical results, we simulate the AFM skyrmion motion using a two-sublattice LLG equation:

$$\frac{\partial \mathbf{m}_i}{\partial t} = -\frac{\gamma}{1+\alpha^2}\mathbf{m}_i \times \boldsymbol{H}_{\text{eff},\,i} - \frac{\alpha\gamma}{1+\alpha^2}\mathbf{m}_i \times (\mathbf{m}_i \times \boldsymbol{H}_{\text{eff},\,i}) \; (i = A, B). \tag{26}$$

Here γ is the gyromagnetic ratio, and $\mathbf{m}_i$ is the normalized magnetization on each sublattice. The effective field $\mathbf{H}_{\text{eff},i}$ includes all the contributions outlined in Eq. (2), obtained from the respective energy contributions. The magneto-elastic coupling term is obtained from the following energy density expression [112]

$$\begin{aligned} \mathrm{U}_{\text{mel},i} = {} & B_1[(\mathbf{m_i}\cdot\mathbf{e}_1)^2(\mathbf{S}_d\cdot\mathbf{e}_1) + (\mathbf{m_i}\cdot\mathbf{e}_2)^2(\mathbf{S}_d\cdot\mathbf{e_2}) \\ & + (\mathbf{m_i}\cdot\mathbf{e}_3)^2(\mathbf{S}_d\cdot\mathbf{e}_3)] \\ & + 2B_2[(\mathbf{m_i}\cdot\mathbf{e}_1)(\mathbf{m_i}\cdot\mathbf{e}_2)(\mathbf{S}_{od}\cdot\mathbf{e}_3) \\ & + (\mathbf{m_i}\cdot\mathbf{e}_1)(\mathbf{m_i}\cdot\mathbf{e}_3)(\mathbf{S}_{od}\cdot\mathbf{e}_2) \\ & + (\mathbf{m_i}\cdot\mathbf{e}_2)(\mathbf{m_i}\cdot\mathbf{e}_3)(\mathbf{S}_{od}\cdot\mathbf{e}_1)]. \end{aligned} \tag{27}$$

Here B_1, B_2 are magneto-elastic coefficients (taken as 25 MJ/m^3), $\mathbf{e}_1$, $\mathbf{e}_2$, $\mathbf{e}_3$ are cubic axes (taken as **x**, **y**, **z**), $\mathbf{S}_d = (S_{xx},\ S_{yy},\ S_{zz})$, and $\mathbf{S}_{od} = (S_{yz},\ S_{xz},\ S_{xy})$ are the symmetric strain tensor components. While the model validity investigated here does not depend on the strength of magneto-elastic coupling, large coupling values are possible, for example, in thin-film antiferromagnetic NiO [113]. The strain is calculated by solving the elastodynamics wave equation:

$$\rho\frac{\partial^2\mathbf{u}}{\partial t^2} = \mathbf{f} - \eta\frac{\partial \mathbf{u}}{\partial t}, \tag{28}$$

where ρ is the mass density, η is the mechanical damping (energy dissipation term), **u** is the mechanical displacement, and **f** is the body force density with components obtained from the symmetric stress tensor $\boldsymbol{\sigma}$ as

$$f_p = \sum_{q=1}^{3}\frac{\partial \sigma_{pq}}{\partial x_q} \; (p = x, y, z). \tag{29}$$

The stress and strain components are related using elastic stiffness coefficients for a cubic crystal $c_{11}c_{12}$, and c_{44} as

$$\boldsymbol{\sigma}_d = \begin{pmatrix} c_{11} & c_{12} & c_{12} \\ c_{12} & c_{11} & c_{12} \\ c_{12} & c_{12} & c_{11} \end{pmatrix}\boldsymbol{S}_d, \quad \boldsymbol{\sigma}_{od} = \begin{pmatrix} c_{44} & 0 & 0 \\ 0 & c_{44} & 0 \\ 0 & 0 & c_{44} \end{pmatrix}\boldsymbol{S}_{od}. \tag{30}$$

Here we take $\rho = 8740$ kg/m^3, $c_{11} = 300$ GN/m^2, $c_{12} = 200$ GN/m^2, $c_{44} = 50$ GN/m^2, giving a longitudinal elastic wave velocity of $\mathrm{v}_{||} \cong 4400$ m/s. At boundaries with surface normal direction $\mathbf{n}_q$ $(q = x, y, z)$, the stress is related to external pressure **F** components by (δ is the Kronecker delta)

$$\sum_{l=1}^{3}\delta_{pl}\sigma_{ql} = F_p \; (p = x, y, z). \tag{31}$$

A surface acoustic wave of wavelength $\lambda = v_{||}/f$, is generated using IDTs, as shown in Fig. 2 on the top track surface, such that the electrode width and spacing are $\lambda/4$ (IDT period of λ), each generating an external shear pressure along the y direction as $\pm F\sin(2\pi ft)$, alternating in sign between electrodes, and with amplitude $F = 5\times10^7$ N/m^2. Using a mechanical damping constant $\eta = 3\times10^{13}$ kg m^{-3} s^{-1}, this results in a damped linear wave with longitudinal strain component $S_{yy} = A\sin(2\pi(v_{||}t - y)/\lambda)\exp(-y/L)$, where $L = 2\ \mu$m and $A = 10^{-3}$, and transverse component $S_{zz} = -S_{yy}/2$. To avoid wave reflections from the far end of the track, an absorbing section is defined over the final 100 nm length, where the mechanical damping increases by a factor of 10^3 using a tanh profile of 25 nm width. This results in rapid absorption of the SAW with no back-reflection, and consequently the length of simulated track does not affect skyrmion motion. The elastodynamics wave equation is solved in the velocity-stress representation using the finite-difference time-domain method [114], with the bottom track surface fixed, while the LLG equation is solved using the RK4 method. The cell size used was 2.5 nm, and the time step was 100 fs for both the

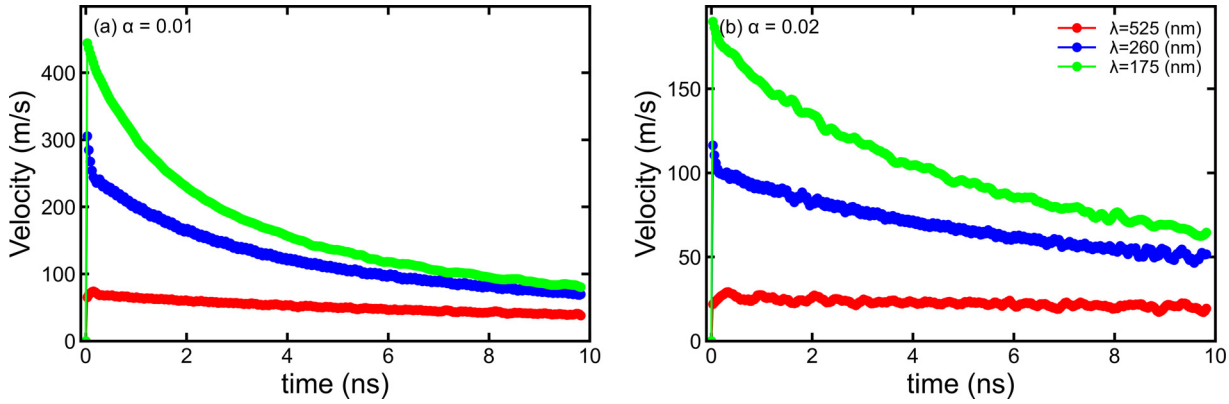

FIG. 7. Skyrmion velocity as a function of time, computed numerically for linear waves with wavelengths $\lambda = 175$, 260, and 525 nm, and magnetic damping parameters of (a) $\alpha = 0.01$ and (b) $\alpha = 0.02$.

LLG and wave equations. The results are plotted in Fig. 6, showing the skyrmion displacement as a function of time for different wavelength values and magnetic damping parameters $\alpha = 0.01$ and 0.02, obtained for a skyrmion with diameter $\cong$20 nm. These results may be compared with the analytical model results in Fig. 4. Qualitatively, a good agreement is obtained between the analytical and numerical models, confirming the increase in total displacement with decreasing wavelength, as well as reduction in total displacement with increasing magnetic damping. Moreover, the skyrmion motion is highly nonlinear, decelerating after the initial fast displacement as also obtained by the analytical model, due to energy dissipation, modeled through the mechanical damping parameter η in the numerical model.

A reasonable quantitative agreement is also obtained, although an exact agreement is difficult due to additional effects present in the numerical simulation, not captured in the analytical model. The main source of discrepancy is the malleable nature of the skyrmion, which varies in diameter periodically with the elastic wave owing to the periodic modification of the total effective anisotropy, resulting in a diameter oscillation of $\pm$8 nm. Thus, while the displacement is monotonically increasing with time, the skyrmion velocity shows periodic fluctuations correlated with the SAW frequency. The numerical results confirm the analytical model, which is strictly applicable in the limit of rigid skyrmions. It should be noted the skyrmion remains in a disk-like shape, with minimal distortion throughout the motion. When skyrmions are highly distorted, it is known that, in synthetic antiferromagnets, a flexo-Hall effect arises, so the skyrmion Hall angle is not zero [115,116]. This is not the case here because the skyrmion does not undergo distortion and, consequently, the skyrmion Hall angle is zero, as expected in an antiferromagnet. There is also a good, qualitative and quantitative, consistency between Figs. 7 and 3 for $\lambda = 525$ nm and consequently for other wavelengths. That is, the numerical calculations verify the theoretical findings. After the energy and momentum transfer between the wave and skyrmion, its velocity rises abruptly and reaches the highest value, then it descends and goes to a constant value asymptotically. The skyrmion dynamics has been shown for one sublattice in the Supplemental Material [117]. The skyrmion displacement animation, showing the z-direction magnetization on sublattice A (red magnetization out of the plane, blue into the plane), is obtained for $l = 260$ nm and $\alpha = 0.01$.

IV. SUMMARY AND CONCLUSION

In summary, we have investigated the dynamics of AFM skyrmions induced by surface acoustic waves through the Born approximation scattering approach. It was shown that the skyrmion motion is inversely proportional to Gilbert damping both in linear and circular-wave polarization. It moves exactly in the straight line with no ratchet motion in the existence of linear waves, as expected. This fact corresponds to zero Hall angle for skyrmions in AFM systems, since there is no torque exerted by the linear wave. The linear velocity, depending on the potential strength and damping induced by the linear wave reaches to 200–250 m/s in the highest magnitude. For circular waves, the amount of applied force is half of the linear wave's force, however, there is a nonzero torque magnitude. This torque changes the behavior of skyrmion dynamics and results in an ultrafast ratchet motion of the texture. The angular momentum of the circular wave gives rise to an ultrafast rotation of the skyrmion, whose direction may be reversed by changing the incident wave helicity, and is of the terahertz order. Numerical calculations have been performed using BORIS computational spintronics [112] for a two-sublattice AFM system. The simulation results show a good agreement with theoretical predictions for linear waves. All in all, the motion of skyrmion in AFM systems stimulated with a surface wave is in a straight line, rotates around central axis, and has no skyrmion Hall effect.

ACKNOWLEDGMENT

We acknowledge fruitful discussions with S. K. Kim, O. Tretiakov, M. Hamdi, and E. Nedaee.

[1] V. Baltz, A. Manchon, M. Tsoi, T. Moriyama, T. Ono, and Y. Tserkovnyak, Rev. Mod. Phys. **90**, 015005 (2018).

[2] T. Jungwirth, J. Sinova, A. Manchon, X. Marti, J. Wunderlich, and C. Felser, Nat. Phys. **14**, 200 (2018).

[3] P. Ross, M. Schreier, J. Lotze, H. Huebl, R. Gross, and S. T. Goennenwein, J. Appl. Phys. **118**, 233907 (2015).
[4] O. Gomonay, V. Baltz, A. Brataas, and Y. Tserkovnyak, Nat. Phys. **14**, 213 (2018).
[5] T. Jungwirth, X. Marti, P. Wadley, and J. Wunderlich, Nat. Nanotechnol. **11**, 231 (2016).
[6] E. Gomonay and V. Loktev, Low Temp. Phys. **40**, 17 (2014).
[7] A. MacDonald and M. Tsoi, Philos. Trans. R. Soc., A **369**, 3098 (2011).
[8] X. Martí, I. Fina, and T. Jungwirth, IEEE Trans. Magn. **51**, 1 (2015).
[9] L. Néel, Ann. Phys. (Paris, Fr.), **11**, 232 (1936).
[10] F. Bitter, Phys. Rev. **54**, 79 (1938).
[11] J. Logan, H. Kim, D. Rosenmann, Z. Cai, R. Divan, O. G. Shpyrko, and E. Isaacs, Appl. Phys. Lett. **100**, 192405 (2012).
[12] P. Wadley, S. Reimers, M. J. Grzybowski, C. Andrews, M. Wang, J. S. Chauhan, B. L. Gallagher, R. P. Campion, K. W. Edmonds, S. S. Dhesi *et al.*, Nat. Nanotechnol. **13**, 362 (2018).
[13] S. Selzer, U. Atxitia, U. Ritzmann, D. Hinzke, and U. Nowak, Phys. Rev. Lett. **117**, 107201 (2016).
[14] E. G. Tveten, A. Qaiumzadeh, O. A. Tretiakov, and A. Brataas, Phys. Rev. Lett. **110**, 127208 (2013).
[15] I. Dzyaloshinsky, J. Phys. Chem. Solids **4**, 241 (1958).
[16] T. Moriya, Phys. Rev. **120**, 91 (1960).
[17] K. Ahmadi, F. Mahfouzi, L. Jamilpanah, M. Mohseni, T. Böttcher, P. Pirro, N. Kioussis, J. Åkerman, S. Seyyed Ebrahimi, and S. M. Mohseni, Sci. Rep. **12**, 11877 (2022).
[18] A. Tonomura, X. Yu, K. Yanagisawa, T. Matsuda, Y. Onose, N. Kanazawa, H. S. Park, and Y. Tokura, Nano Lett. **12**, 1673 (2012).
[19] X. Yu, N. Kanazawa, Y. Onose, K. Kimoto, W. Zhang, S. Ishiwata, Y. Matsui, and Y. Tokura, Nat. Mater. **10**, 106 (2011).
[20] H. Wilhelm, M. Baenitz, M. Schmidt, U. K. Rößler, A. A. Leonov, and A. N. Bogdanov, Phys. Rev. Lett. **107**, 127203 (2011).
[21] N. Bazazzadeh, M. Hamdi, F. Haddadi, A. Khavasi, A. Sadeghi, and S. M. Mohseni, Phys. Rev. B **103**, 014425 (2021).
[22] S. Heinze, K. Von Bergmann, M. Menzel, J. Brede, A. Kubetzka, R. Wiesendanger, G. Bihlmayer, and S. Blügel, Nat. Phys. **7**, 713 (2011).
[23] M. Bode, M. Heide, K. Von Bergmann, P. Ferriani, S. Heinze, G. Bihlmayer, A. Kubetzka, O. Pietzsch, S. Blügel, and R. Wiesendanger, Nature (London) **447**, 190 (2007).
[24] X. Zhang, Y. Zhou, and M. Ezawa, Sci. Rep. **6**, 24795 (2016).
[25] T. Dohi, S. DuttaGupta, S. Fukami, and H. Ohno, Nat. Commun. **10**, 5153 (2019).
[26] W. Legrand, D. Maccariello, F. Ajejas, S. Collin, A. Vecchiola, K. Bouzehouane, N. Reyren, V. Cros, and A. Fert, Nat. Mater. **19**, 34 (2020).
[27] K. Ahmadi, L. Jamilpanah, S. A. S. Ebrahimi, A. Olyaee, M. M. Tehranchi, and S. M. Mohseni, J. Phys. D: Appl. Phys. **53**, 465001 (2020).
[28] A. Belavin and A. Polyakov, JETP Lett. **22**, 245 (1975).
[29] A. N. Bogdanov and D. A. Yablonskii, Zh. Eksp. Teor. Fiz. **95**, 178 (1989).
[30] A. Bogdanov and A. Hubert, J. Magn. Magn. Mater. **138**, 255 (1994).
[31] A. Bogdanov and A. Hubert, J. Magn. Magn. Mater. **195**, 182 (1999).
[32] Y. Tchoe and J. H. Han, Phys. Rev. B **85**, 174416 (2012).
[33] Y. Liu, G. Yin, J. Zang, J. Shi, and R. K. Lake, Appl. Phys. Lett. **107**, 152411 (2015).
[34] C. Jin, Z.-A. Li, A. Kovács, J. Caron, F. Zheng, F. N. Rybakov, N. S. Kiselev, H. Du, S. Blügel, M. Tian *et al.*, Nat. Commun. **8**, 15569 (2017).
[35] S. Rohart and A. Thiaville, Phys. Rev. B **88**, 184422 (2013).
[36] R. Juge, S.-G. Je, D. de Souza Chaves, S. Pizzini, L. D. Buda-Prejbeanu, L. Aballe, M. Foerster, A. Locatelli, T. O. Menteş, A. Sala *et al.*, J. Magn. Magn. Mater. **455**, 3 (2018).
[37] D. Cortés-Ortuño, N. Romming, M. Beg, K. von Bergmann, A. Kubetzka, O. Hovorka, H. Fangohr, and R. Wiesendanger, Phys. Rev. B **99**, 214408 (2019).
[38] R. Novak, F. Garcia, E. Novais, J. Sinnecker, and A. Guimaraes, J. Magn. Magn. Mater. **451**, 749 (2018).
[39] R. Khoshlahni, A. Qaiumzadeh, A. Bergman, and A. Brataas, Phys. Rev. B **99**, 054423 (2019).
[40] A. Fert, V. Cros, and J. Sampaio, Nat. Nanotechnol. **8**, 152 (2013).
[41] X. Zhang, Y. Zhou, M. Ezawa, G. P. Zhao, and W. Zhao, Sci. Rep. **5**, 11369 (2015).
[42] Y. Zhou and M. Ezawa, Nat. Commun. **5**, 4652 (2014).
[43] J. Iwasaki, M. Mochizuki, and N. Nagaosa, Nat. Nanotechnol. **8**, 742 (2013).
[44] X. Zhang, G. P. Zhao, H. Fangohr, J. P. Liu, W. X. Xia, J. Xia, and F. J. Morvan, Sci. Rep. **5**, 7643 (2015).
[45] J. Sampaio, V. Cros, S. Rohart, A. Thiaville, and A. Fert, Nat. Nanotechnol. **8**, 839 (2013).
[46] N. Bazazzadeh, M. Hamdi, S. Park, A. Khavasi, S. M. Mohseni, and A. Sadeghi, Phys. Rev. B **104**, L180402 (2021).
[47] S. A. Montoya, R. Tolley, I. Gilbert, S.-G. Je, M.-Y. Im, and E. E. Fullerton, Phys. Rev. B **98**, 104432 (2018).
[48] R. H. Liu, W. L. Lim, and S. Urazhdin, Phys. Rev. Lett. **114**, 137201 (2015).
[49] R. Tomasello, E. Martinez, R. Zivieri, L. Torres, M. Carpentieri, and G. Finocchio, Sci. Rep. **4**, 6784 (2014).
[50] L. Kong and J. Zang, Phys. Rev. Lett. **111**, 067203 (2013).
[51] C. Gong, Y. Zhou, and G. Zhao, Appl. Phys. Lett. **120**, 052402 (2022).
[52] S. Komineas and N. Papanicolaou, Phys. Rev. B **92**, 064412 (2015).
[53] L. Shen, J. Xia, G. Zhao, X. Zhang, M. Ezawa, O. A. Tretiakov, X. Liu, and Y. Zhou, Phys. Rev. B **98**, 134448 (2018).
[54] S. K. Kim, D. Hill, and Y. Tserkovnyak, Phys. Rev. Lett. **117**, 237201 (2016).
[55] M. T. Bryan, J. Dean, and D. A. Allwood, Phys. Rev. B **85**, 144411 (2012).
[56] J. Dean, M. Bryan, J. Cooper, A. Virbule, J. Cunningham, and T. Hayward, Appl. Phys. Lett. **107**, 142405 (2015).
[57] R. Nepal, U. Güngördü, and A. A. Kovalev, Appl. Phys. Lett. **112**, 112404 (2018).
[58] A. Thiele, Phys. Rev. Lett. **30**, 230 (1973).
[59] M. Weißenhofer, L. Rózsa, and U. Nowak, Phys. Rev. Lett. **127**, 047203 (2021).
[60] S. Woo, K. Litzius, B. Krüger, M.-Y. Im, L. Caretta, K. Richter, M. Mann, A. Krone, R. M. Reeve, M. Weigand *et al.*, Nat. Mater. **15**, 501 (2016).

[61] X. Li, L. Shen, Y. Bai, J. Wang, X. Zhang, J. Xia, M. Ezawa, O. A. Tretiakov, X. Xu, M. Mruczkiewicz *et al.*, npj Comput. Mater. **6**, 169 (2020).

[62] M. Sapozhnikov, D. Tatarskiy, and V. Mironov, J. Magn. Magn. Mater. **549**, 169043 (2022).

[63] N. Kent, N. Reynolds, D. Raftrey, I. T. Campbell, S. Virasawmy, S. Dhuey, R. V. Chopdekar, A. Hierro-Rodriguez, A. Sorrentino, E. Pereiro *et al.*, Nat. Commun. **12**, 1562 (2021).

[64] X. S. Wang, A. Qaiumzadeh, and A. Brataas, Phys. Rev. Lett. **123**, 147203 (2019).

[65] A. N. Bogdanov, U. K. Rossler, M. Wolf, and K. H. Müller, Phys. Rev. B **66**, 214410 (2002).

[66] L. D. Landau and E. M. Lifshitz, *Statistical Physics: Vol. 5: Course of Theoretical Physics* (Pergamon Press, 1968).

[67] B. Ivanov, Low Temp. Phys. **40**, 91 (2014).

[68] Q. Pankhurst, C. Johnson, and M. Thomas, J. Phys. C: Solid State Phys. **19**, 7081 (1986).

[69] A. H. Morrish, *Canted Antiferromagnetism: Hematite* (World Scientific, 1994).

[70] P. Bak and M. H. Jensen, J. Phys. C: Solid State Phys. **13**, L881 (1980).

[71] O. Nakanishi, A. Yanase, A. Hasegawa, and M. Kataoka, Solid State Commun. **35**, 995 (1980).

[72] B. Lebech, J. Bernhard, and T. Freltoft, J. Phys.: Condens. Matter **1**, 6105 (1989).

[73] K. Adachi, N. Achiwa, and M. Mekata, J. Phys. Soc. Jpn. **49**, 545 (1980).

[74] T. Ohyama and A. E. Jacobs, Phys. Rev. B **52**, 4389 (1995).

[75] S. Maruyama, H. Tanaka, Y. Narumi, K. Kindo, H. Nojiri, M. Motokawa, and K. Nagata, J. Phys. Soc. Jpn. **70**, 859 (2001).

[76] A. Zheludev, G. Shirane, Y. Sasago, N. Koide, and K. Uchinokura, Phys. Rev. B **54**, 15163 (1996).

[77] A. Zheludev, G. Shirane, Y. Sasago, N. Koide, and K. Uchinokura, Phys. Rev. B **55**, 11879 (1997).

[78] A. Zheludev, S. Maslov, G. Shirane, Y. Sasago, N. Koide, and K. Uchinokura, Phys. Rev. Lett. **78**, 4857 (1997).

[79] M. D. Lumsden, B. C. Sales, D. Mandrus, S. E. Nagler, and J. R. Thompson, Phys. Rev. Lett. **86**, 159 (2001).

[80] A. Zheludev, S. Maslov, G. Shirane, I. Tsukada, T. Masuda, K. Uchinokura, I. Zaliznyak, R. Erwin, and L. P. Regnault, Phys. Rev. B **59**, 11432 (1999).

[81] A. N. Bogdanov, Sov. J. Low Temp. Phys. **12**, 290 (1986).

[82] E. G. Tveten, T. Müller, J. Linder, and A. Brataas, Phys. Rev. B **93**, 104408 (2016).

[83] S. Muhlbauer, B. Binz, F. Jonietz, C. Pfleiderer, A. Rosch, A. Neubauer, R. Georgii, and P. Boni, Science **323**, 915 (2009).

[84] I. Kézsmárki, S. Bordács, P. Milde, E. Neuber, L. Eng, J. White, H. M. Rønnow, C. Dewhurst, M. Mochizuki, K. Yanai *et al.*, Nat. Mater. **14**, 1116 (2015).

[85] I. Bar'yakhtar and B. Ivanov, Solid State Commun. **34**, 545 (1980).

[86] F. D. M. Haldane, Phys. Rev. Lett. **50**, 1153 (1983).

[87] A. F. Andreev and V. I. Marchenko, Sov. Phys. Usp. **23**, 21 (1980).

[88] M. Kardar, *Statistical Physics of Fields* (Cambridge University Press, 2007).

[89] E. G. Tveten, A. Qaiumzadeh, and A. Brataas, Phys. Rev. Lett. **112**, 147204 (2014).

[90] T. Shiino, S.-H. Oh, P. M. Haney, S.-W. Lee, G. Go, B.-G. Park, and K.-J. Lee, Phys. Rev. Lett. **117**, 087203 (2016).

[91] K. M. D. Hals, Y. Tserkovnyak, and A. Brataas, Phys. Rev. Lett. **106**, 107206 (2011).

[92] S. A. Bender, H. Skarsvåg, A. Brataas, and R. A. Duine, Phys. Rev. Lett. **119**, 056804 (2017).

[93] H. Velkov, O. Gomonay, M. Beens, G. Schwiete, A. Brataas, J. Sinova, and R. A. Duine, New J. Phys. **18**, 075016 (2016).

[94] E. Galkina and B. Ivanov, Low Temp. Phys. **44**, 618 (2018).

[95] B. Ivanov, Low Temp. Phys. **31**, 635 (2005).

[96] A. Qaiumzadeh, L. A. Kristiansen, and A. Brataas, Phys. Rev. B **97**, 020402(R) (2018).

[97] N. Nagaosa and Y. Tokura, Nat. Nanotechnol. **8**, 899 (2013).

[98] X. S. Wang, H. Y. Yuan, and X. R. Wang, Commun. Phys. **1**, 31 (2018).

[99] H.-B. Braun, Phys. Rev. B **50**, 16485 (1994).

[100] L. Zhang and Q. Niu, Phys. Rev. Lett. **112**, 085503 (2014).

[101] A. Sytcheva, U. Löw, S. Yasin, J. Wosnitza, S. Zherlitsyn, P. Thalmeier, T. Goto, P. Wyder, and B. Lüthi, Phys. Rev. B **81**, 214415 (2010).

[102] J. J. Sakurai and E. D. Commins, *Modern Quantum Mechanics, Revised Edition* (Addison-Wesley, 1995).

[103] W. M. Haynes, D. R. Lide, and T. J. Bruno, *CRC Handbook of Chemistry and Physics* (CRC Press, 2016).

[104] N. Romming, C. Hanneken, M. Menzel, J. E. Bickel, B. Wolter, K. von Bergmann, A. Kubetzka, and R. Wiesendanger, Science **341**, 636 (2013).

[105] N. Romming, A. Kubetzka, C. Hanneken, K. von Bergmann, and R. Wiesendanger, Phys. Rev. Lett. **114**, 177203 (2015).

[106] E. Simon, K. Palotás, L. Rózsa, L. Udvardi, and L. Szunyogh, Phys. Rev. B **90**, 094410 (2014).

[107] S. Jaiswal, K. Litzius, I. Lemesh, F. Büttner, S. Finizio, J. Raabe, M. Weigand, K. Lee, J. Langer, B. Ocker *et al.*, Appl. Phys. Lett. **111**, 022409 (2017).

[108] W. Jiang, P. Upadhyaya, W. Zhang, G. Yu, M. B. Jungfleisch, F. Y. Fradin, J. E. Pearson, Y. Tserkovnyak, K. L. Wang, O. Heinonen *et al.*, Science **349**, 283 (2015).

[109] J. Barker and O. A. Tretiakov, Phys. Rev. Lett. **116**, 147203 (2016).

[110] W. Chen, L. Liu, and Y. Zheng, Phys. Rev. Appl. **14**, 064014 (2020).

[111] D.-H. Kim, D.-H. Kim, K.-J. Kim, K.-W. Moon, S. Yang, K.-J. Lee, and S. K. Kim, J. Magn. Magn. Mater. **514**, 167237 (2020).

[112] S. Lepadatu, J. Appl. Phys. **128**, 243902 (2020).

[113] C. Schmitt *et al.*, arXiv:2209.02040v1.

[114] J. Virieux, Geophysics **49**, 1933 (1984).

[115] P. E. Roy, R. M. Otxoa, and C. Moutafis, Phys. Rev. B **99**, 094405 (2019).

[116] L. Liu, W. Chen, and Y. Zheng, Phys. Rev. Lett. **128**, 257201 (2022).

[117] See Supplemental Material at http://link.aps.org/supplemental/10.1103/PhysRevB.107.144421 for a movie of the skyrmion motion induced by linear surface acoustic wave. This movie shows the skyrmion motion only in one sublattice, such as sublattice A.